



# The catalytic activity of microporous and mesoporous NiCoBeta zeolite catalysts in Fischer–Tropsch synthesis

Karolina A. Chalupka<sup>1</sup> · Renata Sadek<sup>1,2</sup> · Lukasz Szkudlarek<sup>1</sup> · Pawel Mierczynski<sup>1</sup> · Waldemar Maniukiewicz<sup>1</sup> · Jacek Rynkowski<sup>1</sup> · Jacek Gurgul<sup>3</sup> · Sandra Casale<sup>2</sup> · Dalil Brouiri<sup>2</sup> · Stanislaw Dzwigaj<sup>2</sup>

Received: 24 October 2020 / Accepted: 28 November 2020 / Published online: 18 January 2021  
© Springer Nature B.V. 2021

## Abstract

Two kinds of microporous and mesoporous NiCoBeta zeolite catalysts were prepared. The effect of bimetallic zeolite preparation method, dealumination degree, the presence of micropores in the support structure and the effect of nickel addition on the activity and selectivity of cobalt-based microporous and mesoporous dealuminated and non-dealuminated zeolite catalysts in Fischer–Tropsch synthesis were determined. These catalysts were obtained by sequential impregnation ( $\text{Ni}_{3.0}\text{Co}_{20}\text{AlBeta}$  and  $\text{Ni}_{3.0}\text{Co}_{20}\text{SiBeta}$ ) and co-impregnation ( $\text{co-Ni}_{3.0}\text{Co}_{20}\text{AlBeta}$  and  $\text{co-Ni}_{3.0}\text{Co}_{20}\text{SiBeta}$ ). The study showed that the presence of Ni leads to a lower cobalt oxide reduction temperature and an increase in CO conversion. Nickel–cobalt zeolite systems showed high activity and selectivity throughout the lifetime of the reaction. The use of a two-step post-synthesis method and the promotion of cobalt systems with nickel allow to obtain active, selective, and stable zeolite catalysts for Fischer–Tropsch synthesis.

**Keywords** Fischer–Tropsch synthesis · Beta zeolite · Bimetallic Ni–Co catalysts · XPS

**Electronic supplementary material** The online version of this article (<https://doi.org/10.1007/s11164-020-04343-0>) contains supplementary material, which is available to authorized users.

✉ Karolina A. Chalupka  
karolina.chalupka@p.lodz.pl

✉ Stanislaw Dzwigaj  
stanislaw.dzwigaj@sorbonne-universite.fr

Extended author information available on the last page of the article

## Introduction

Fischer–Tropsch synthesis is one of the most important reactions in ecological fuel production. For many years, the researchers were searching and still they are looking for solutions for optimizing Fischer–Tropsch synthesis (FTS) and designing of FTS catalysts. Scientists are focused on controlling the product selectivity and resistance to carbon deposition formation because it is a serious problem in FTS process and causes deactivation of catalysts which leads to decrease in the activity and selectivity of used catalysts. The activity of catalysts in FTS depends on their composition, preparation methods, conditions of catalysts activation (reduction temperature, reduction medium etc.) [1, 2]. The performance of FTS catalysts plays a crucial role in its industrial applications [3]. All metals from group VIII of periodic table have some activity in the C–C coupling reaction during FTS and the highest activity present Fe, Co, Ni and Ru [4–6]. It is important to say that only Fe- and Co-based catalysts are used for industrial processes due to their high activity, selectivity, and low cost [7, 8]. Other active metals like Ni and Ru have been applied only as promoters for iron- and cobalt-based catalysts [9–11].

The supported cobalt catalysts are the most popular catalyst for FTS process, and they are widely used because they can work at low temperature. Moreover, they possess high activity and selectivity to longer chain hydrocarbons, and very high resistance to water. However, they have also some disadvantages like they will lead to a complex and expensive downstream processing unit to make further processing such as isomerization and cracking. For this reason, the catalysts with binary or ternary cobalt metal alloy are seemed to be promising in simultaneously increasing the specific selectivity of certain hydrocarbon fractions [12, 13], and possessing relative lower FT activation energy [14, 15]. Moreover, to the active metal alloy, support is also found to be important to the resultant product distribution [16].

It was proved that bimetallic catalysts exhibited higher activities and enhanced selectivity to heavy hydrocarbons compared with pure metal catalysts. The ratio of metals constituting the bimetallic catalysts is the key factor which strongly influences their properties [17]. Van Helden et al. [18] showed in nickel–cobalt systems that in the case of low Ni contents ( $\text{Co/Ni} > 3$ ), increasing the amount of this metal does not change the selectivity to methane and  $\text{C}_{5+}$  hydrocarbons. However, at higher nickel concentrations, there is a significant decrease in the amount of heavier hydrocarbons formed which may be related to a lower concentration of  $\text{CH}_x$  species on the alloy surfaces or to an increase in the surface concentration of hydrogen.

It was found that a certain kind of catalyst containing Ni could be developed to obtain the co-production of methane and gasoline. FTS reaction catalyzed by this catalyst would increase the selectivity of its gas product and thus provide substitutes for both natural gas and crude oil [19].

Many literature data prove that zeolite-cobalt containing catalysts may be promised catalysts for FTS and the Si/Al ratio and structural type of zeolite may allow to control the distribution of forming product in this process and may lead to obtain light synthetic oil or fuel fraction [3, 20]. The present work was undertaken to study the performance of bimetallic catalyst of Co and Ni supported on

two types of Beta zeolites (microporous (Mi) and mesoporous (Me) Beta zeolite). It was expected to gain higher activity than for monometallic cobalt Beta zeolite catalysts. The particular emphasis is placed on determination of the best preparation method (sequential impregnation and co-impregnation) of NiCoBeta zeolites and on investigation of dealumination process of Beta zeolites to maximize the benefits of bimetallic Co–Ni catalysts. In this work the physicochemical properties and activity of Me–Ni<sub>3.0</sub>Co<sub>20</sub>Beta and Mi–Ni<sub>3.0</sub>Co<sub>20</sub>Beta zeolites were studied. This is a second part of investigations related to activity and possible application in FTS of bimetallic NiCoBeta zeolites. The first part was recently published on Me–Ni<sub>3.0</sub>Co<sub>10</sub>Beta and Mi–Ni<sub>3.0</sub>Co<sub>10</sub>Beta systems [21].

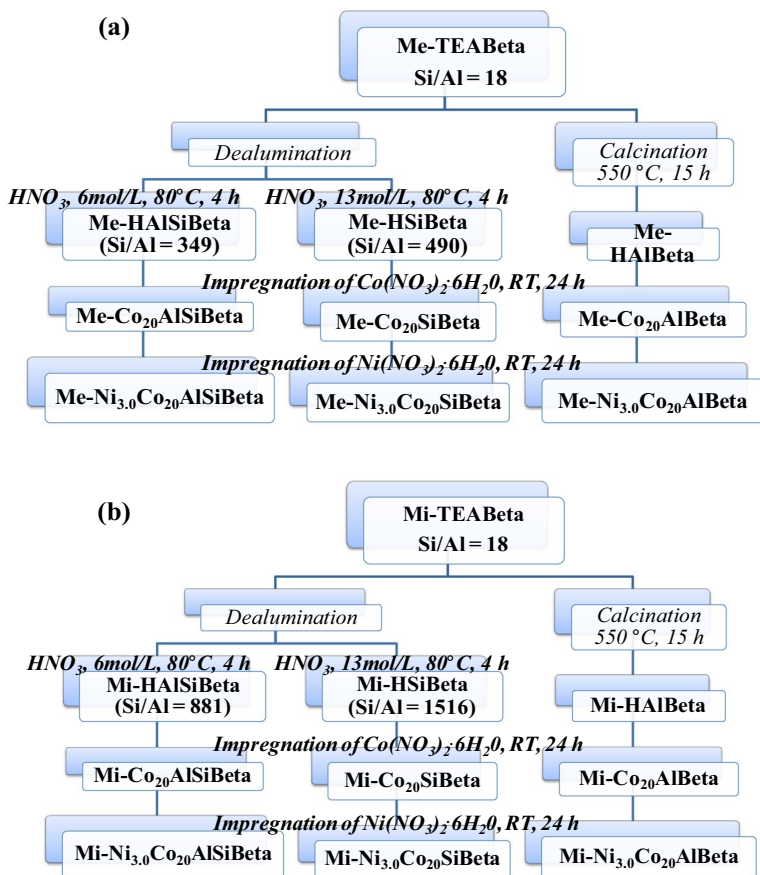
## Methods and materials

### Samples preparation

The NiCoBeta catalysts based on two different kinds of BEA zeolite, microporous and mesoporous, were prepared by two various method: classical wet impregnation and two-step post-synthesis method developed earlier by Dzwigaj et al. [22–36]. The parent microporous and mesoporous TEABeta zeolites were divided into three parts and modified in a different way. In the Scheme 1 the consecutive steps of catalysts preparation are presented.

The first parts were calcined at 550 °C for 15 h to obtain organic free mesoporous (Me)-HAlBeta (Scheme 1a) and microporous (Mi)-HAlBeta zeolites (Scheme 1b). The second and third parts of parent zeolites were obtained by post-synthesis method by treating with nitric acid (HNO<sub>3</sub>) with different concentration and stirring at 80 °C for 4 h to prepare partially (concentration of HNO<sub>3</sub>—6 mol L<sup>-1</sup>) and completely (concentration of HNO<sub>3</sub>—13 mol L<sup>-1</sup>) dealuminated supports. These supports were marked as Me-HAlSiBeta, Me-SiBeta (Scheme 1a) and Mi-HAlSiBeta, Mi-SiBeta (Scheme 1b). Such prepared carriers were impregnated by cobalt nitrate (Co(NO<sub>3</sub>)<sub>2</sub> · 6 H<sub>2</sub>O) for 24 h to obtain cobalt Beta zeolites (contained 20 wt% of cobalt) with different Si/Al ratio and then in sequential impregnation the CoBeta samples were treated by nickel nitrate (Ni(NO<sub>3</sub>)<sub>2</sub> · 6 H<sub>2</sub>O). The next steps were water evaporation and calcination at 500 °C for 3 h. In this way, the six various catalysts were prepared and were labelled as Me–Ni<sub>3.0</sub>Co<sub>20</sub>AlBeta, Me–Ni<sub>3.0</sub>Co<sub>20</sub>AlSiBeta, Me–Ni<sub>3.0</sub>Co<sub>20</sub>SiBeta (Scheme 1a) and Mi–Ni<sub>3.0</sub>Co<sub>20</sub>AlBeta, Mi–Ni<sub>3.0</sub>Co<sub>20</sub>AlSiBeta and Mi–Ni<sub>3.0</sub>Co<sub>20</sub>SiBeta (Scheme 1b).

Part of each fraction of the obtained catalytic systems was activated in situ under atmospheric pressure in the flow of the mixture 95 vol% H<sub>2</sub> and 5 vol% Ar at 400 °C, which led to the formation of Red-Ni<sub>3.0</sub>Co<sub>20</sub>AlBeta, Red-Ni<sub>3.0</sub>Co<sub>20</sub>AlSiBeta and Red-Ni<sub>3.0</sub>Co<sub>20</sub>SiBeta.



**Scheme 1** Preparation method of **a** mesoporous and **b** microporous systems

## Methods of samples characterization

The metal content and the Si/Al ratio of tested catalysts were measured by the X-ray Fluorescence (XRF) SPECTRO X-LabPro apparatus at room temperature.

The XRD patterns of catalysts were obtained on PANalytical X'Pert Pro diffractometer using Cu K $\alpha$  radiation ( $\lambda = 154.05$  pm) in  $2\theta$  range of  $5\text{--}90^\circ$  in ambient atmosphere. The phase transformation of catalysts during reduction process at 300 and 400 °C was also determined. These measurements were taken in situ by using the same apparatus equipped with an Anton Paar XRK900 reactor chamber. Approximately 150 mg of sample was packed in the glass ceramic (Macor) XRD sample holder. The reagent gas used in the experiment was a mixture of 5 vol% H<sub>2</sub> and 95 vol% Ar. The sample was heated at a nominal rate of 5 °C min<sup>-1</sup>. The X-ray source was a copper long fine focus X-ray diffraction tube operating at 40 kV and 30 mA. The patterns were collected in the  $2\theta$  range of  $5\text{--}80^\circ$  (step 0.0167°, 50 s per step).

The X-ray Photoelectron Spectroscopy (XPS) measurements were carried out with a hemispherical analyzer (SES R4000, Gammatdata Scienta). The unmonochromatized Al K $\alpha$  (1486.6 eV) X-ray source with the anode operating at 12 kV and 15 mA current emission was applied to generate core excitation. The energy resolution of the system, measured as a full width at half maximum (FWHM) for Ag 3d<sub>5/2</sub> excitation line, was 0.9 eV (pass energy 100 eV). The spectrometer was calibrated according to ISO 15472:2001. The base pressure in the analysis chamber was about  $2 \times 10^{-9}$  mbar during the experiment. The powder samples were pressed into indium foil and mounted on a dedicated holder. All spectra were collected at pass energy of 100 eV (with 25 meV step) except survey scans which were collected at pass energy of 200 eV (with 0.25 eV step). The area of sample analysis was about 3 mm<sup>2</sup>.

Intensities were estimated by calculating the integral of each peak (CasaXPS 2.3.15), after subtraction of the Shirley-type background, and fitting the experimental curve with a combination of Gaussian and Lorentzian lines of variable proportions (70:30). The Co 2*p* and Ni 2*p* core excitations were deconvoluted with a relative intensity ratio of 2*p*<sub>3/2</sub> and 2*p*<sub>1/2</sub> lines fixed to 2:1. The samples were weakly conductive; thus all binding energy values were charge-corrected to the carbon C 1*s* excitation which set at 285.0 eV.

The temperature-programmed reduction with hydrogen (TPR-H<sub>2</sub>) of cobalt-based catalysts (c.a. 0.08 g) was carried out in the U-shaped tubular quartz microreactor. The flow of reducing mixture of 5% H<sub>2</sub> in Ar was 25 mL min<sup>-1</sup>. The measurement was taken in the temperature range of 30–900 °C with the ramp rate of 10 °C min<sup>-1</sup>. The consumption of hydrogen was monitored by thermal conductivity detector (TCD).

Transmission electron microscope (TEM) images were carried out using JEM-100 CX II ELECTRON MICROSCOPE JEOL. Before the TEM measurement, all reduced samples were ultrasonically dispersed in a pure ethanol and a drop of obtained suspension was deposited on a carbon film on copper grids.

The temperature-programmed desorption of ammonia (NH<sub>3</sub>-TPD) studies were performed in a quartz reactor. Prior to the measurement, the sample was pretreated at 500 °C in the He flow for 30 min. Next, the reactor was cooled down to 100 °C and in this temperature the adsorption of gaseous ammonia was carried out for 15 min. For removal of the physisorbed ammonia from the zeolite surface, the tested systems were flushed with helium flow at 100 °C for 15 min. NH<sub>3</sub>-TPD studies were performed in the temperature range of 40–500 °C. The amount of adsorbed ammonia was detected by thermal conductivity detector. Additionally, in order to check the impact of metal reduction on the acidity of the sample, it was subjected to hydrogen flow at 400 °C for 1 h before performing the adsorption of gaseous ammonia.

## The catalytic test

Before the Fischer–Tropsch synthesis, all tested samples were pretreated at 400 °C in the H<sub>2</sub> flow for 1 h. The reaction was performed at 30 atm and 260 °C. The flow of reactant gas mixture (H<sub>2</sub>/CO=2) was 60 cm<sup>3</sup> min<sup>-1</sup>. For each measurement, 0.5 g sample was loaded in the reactor. The stabilization of reaction conditions

was carried out for 15 h. Gas products were analyzed by GC gas chromatograph (Shimadzu GC-14) equipped with thermal conductivity detector and two columns: measuring—Carbosphere 7A and comparative—molecular sieves 7B. The parameters of operating chromatograph were as follows: column temperature  $-45\text{ }^{\circ}\text{C}$ , detector temperature  $-120\text{ }^{\circ}\text{C}$  and injector temperature  $-120\text{ }^{\circ}\text{C}$ . The following formulas were used to calculate the conversion of CO ( $K_{\text{CO}}$ ) and selectivity to  $\text{CO}_2$  ( $S_{\text{CO}_2}$ ),  $\text{CH}_4$  ( $S_{\text{CH}_4}$ ), and liquid products ( $S_{\text{LP}}$ ):

$$K_{\text{CO}} = \frac{S_{\text{CO}_{\text{in}}} - S_{\text{CO}_{\text{ari}}}}{S_{\text{CO}_{\text{in}}}} \cdot 100\%$$

$$S_{\text{CH}_4} = \frac{X_{\text{CH}_4 i} \cdot 100\%}{X_{\text{CH}_4 \text{out}}} / F$$

$$X_{\text{CH}_4 \text{out}} = \frac{X_{\text{CH}_4 s} \cdot K_{\text{CO}}}{100\%}$$

$$S_{\text{CO}_2 \text{out}} = \frac{X_{\text{CO}_2 i} \cdot 100\%}{X_{\text{CO}_2 \text{out}}} / F$$

$$X_{\text{CO}_2 \text{out}} = \frac{X_{\text{CO}_2 s} \cdot K_{\text{CO}}}{100\%}$$

$$F = \frac{S_{\text{Ar } i}}{S_{\text{Ar } s}}$$

$$S_{\text{LP}} = 100 - (S_{\text{CH}_4} + S_{\text{CO}_2})$$

where:  $K_{\text{CO}}$ —conversion of CO,  $S_{\text{CO}_{\text{in}}}$ —the area of the CO peak before reaction,  $S_{\text{CO}_{\text{ari}}}$ —the area of the CO peak after reaction,  $S_{\text{CH}_4}$ — $\text{CH}_4$  selectivity,  $S_{\text{CO}_2}$ — $\text{CO}_2$  selectivity,  $X_{\text{CH}_4 i}$ —the area of the peak of obtained  $\text{CH}_4$ ,  $X_{\text{CO}_2 i}$ —the area of the peak of obtained  $\text{CO}_2$ ,  $X_{\text{CH}_4 \text{out}}$ —the area of the theoretical  $\text{CH}_4$  peak (when all CO is converted to  $\text{CH}_4$ ),  $X_{\text{CO}_2 \text{out}}$ —the area of the theoretical  $\text{CO}_2$  peak (when all CO is converted to  $\text{CO}_2$ ),  $cX_{\text{CH}_4 s}$ —the area of the standard  $\text{CH}_4$  (when only  $\text{CH}_4$  is tested),  $X_{\text{CO}_2 s}$ —the area of the standard  $\text{CO}_2$  (when only  $\text{CO}_2$  is tested),  $F$ —contraction coefficient,  $S_{\text{Ar } i}$ —the area of the Ar peak during reaction,  $S_{\text{Ar } s}$ —the area of the Ar peak before reaction,  $S_{\text{LP}}$ —liquid products selectivity.

Liquid products were analysed by GC MS (6890 N Network GC System with a Zebtron Phase ZB-1MS capillary column—a length of 30 m, an internal diameter of 0.25 mm linked with a 5973 Network Mass Selective Detector mass spectrometer with a 7683 Series Injector autosampler. The chromatographic

analysis was performed in the temperature range 70–250 °C with temperature rise rate of 8 °C min<sup>-1</sup>. The initial and final temperatures were held for 3 and 30 min, respectively.

## Results and discussion

### The determination of phase composition by XRD technique

XRD patterns for nickel and cobalt modified zeolites are shown in Fig. 1. For all samples, the diffraction lines at  $2\theta$  of approximately 7.8° and 22.4° are determined, which are characteristic for Beta zeolite and indicate the coexistence of two isomorphs of this material. The presented research shows that the crystal structure of the Beta zeolite is preserved, both after the dealumination process as well as the introduction of metal ions (Ni and Co) into the Beta zeolite structure [37, 38]. The characteristic reflections of NiCo<sub>2</sub>O<sub>4</sub> and/or Co<sub>3</sub>O<sub>4</sub> ( $2\theta=36.69^\circ$ ,  $44.56^\circ$ ,  $64.94^\circ$ ) appeared in the NiCoBeta patterns. The appearance of the lines at  $2\theta$  of approximately 59.16° is related to the presence of NiO. In addition, for the Me–Ni<sub>3.0</sub>Co<sub>20</sub>AlBeta, Mi–Ni<sub>3.0</sub>Co<sub>20</sub>AlBeta, and Mi–co–Ni<sub>3.0</sub>Co<sub>20</sub>SiBeta systems, reflexes associated with the presence of NiO are observed, Co<sub>3</sub>O<sub>4</sub> and/or NiCo<sub>2</sub>O<sub>4</sub> [39–42].

The reduction of the nickel–cobalt systems did not cause a significant decrease in the intensity of diffraction peaks characteristic for the Beta zeolite, what suggests that the crystal structure of the support was not destroyed during the reduction

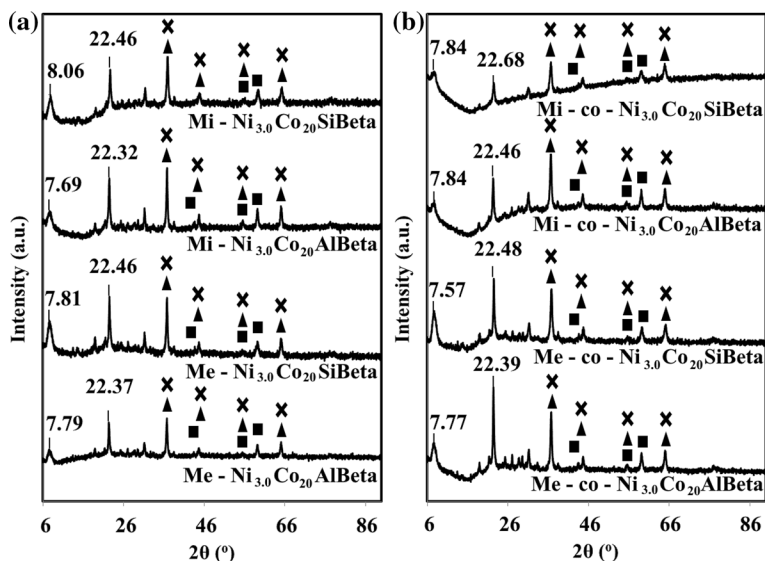


**Fig. 1** XRD patterns obtained for Mi–Ni<sub>3.0</sub>Co<sub>20</sub>Beta (a) and Me–Ni<sub>3.0</sub>Co<sub>20</sub>Beta (b) catalysts prepared by sequential and co-impregnation method after calcination process (Filled Triangle—Co<sub>3</sub>O<sub>4</sub>, Filled Square—NiO, Multiplication—NiCo<sub>2</sub>O<sub>4</sub>)

process and it confirms high stability of the obtained systems (Fig. 2). The XRD diffractograms of the catalysts show additional lines at  $2\theta=44.41^\circ$  and  $75.56^\circ$ , which can be assigned to the presence of the alloy Ni–Co and/or NiO and/or CoO [40, 43]. Due to the almost identical diffraction patterns of cobalt and nickel oxides, it is impossible to distinguish them clearly using the XRD method for such weak reflexes.

## XPS results

The X-ray photoelectron spectra of  $\text{Ni}_3\text{Co}_{20}\text{Beta}$  samples have been analysed numerically in the BE regions of Si  $2p$ , Al  $2p$ , O  $1s$ , C  $1s$ , Ni  $2p$  and Co  $2p$ .

All Si  $2p$  spectra are well fitted by three doublets with the spin–orbit splitting of 0.61 eV (see Supporting Information). Relative intensities of these components do not depend on the porosity of zeolite matrix. The most intense components ( $>91\%$ ) with Si  $2p_{3/2}$  BE values of 103.5–104.1 eV are related to the presence of tetrahedral Si(IV) [44–46]. It is worth mentioning that these values are slightly larger than reported earlier for BEA, MFI and MOR zeolites elsewhere [44–48]. There is a visible increase in area of low-BE component (Si  $2p_{3/2}$  BE of 101.4–101.9 eV) in AlBEA samples, but it is still below 5%. Such low BE is characteristic for silicon in lower than 4+ oxidation state. One can find that the dealumination process can slightly influence the silicon matrix.

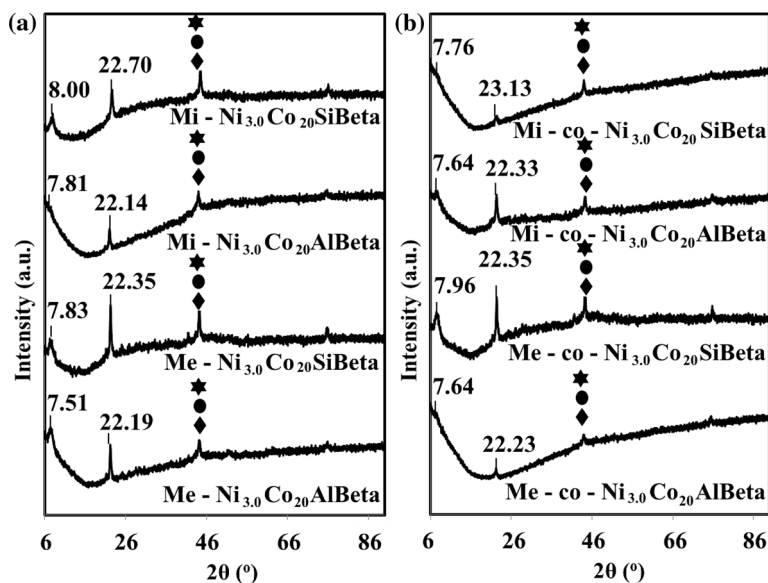


**Fig. 2** XRD patterns obtained for  $\text{Mi-Ni}_{3.0}\text{Co}_{20}\text{Beta}$  (a) and  $\text{Me-Ni}_{3.0}\text{Co}_{20}\text{Beta}$  (b) catalysts prepared by sequential and co-impregnation method after reduction process (Filled diamond— $\text{Ni}^0$ , Filled circle— $\text{Co}^0$ , Filled Star—Ni–Co alloy)

The binding energy of all Al  $2p_{3/2}$  peaks is close to 75.0 eV which is related to  $Al^{3+}$  species ( $Al_2O_3$  BE = 74.9 eV [49]).

The O  $1s$  region can reasonably be decomposed into four components: (i) a main peak located at 533.0–533.4 eV assigned to oxygen in the zeolite framework (Si–O–Si bonds) [50–52]; (ii) two peaks at 529.9–531.4 eV due to oxygen–metal bonds; (iii) a peak at BE higher than 534.6 eV assigned to adsorbed water, OH groups and/or oxygen of organic contaminants. According to our earlier paper [53], we can identify Co–O bonds with BE ~529.9 eV and Ni–O bonds with BE ~531.3 eV. The component with BE = 531.3 eV is related to  $NiCo_2O_4$  (531.2 eV [54]) or  $Ni(OH)_2$  (531.1 eV [55]).

The C  $1s$  core lines generally consist of three peaks at 285.0 eV (organic contaminants), 286.0–286.2 eV (C–O groups) and >289 eV (C=O groups).

Two nickel species have been identified in Ni  $2p$  XPS spectra of all zeolites under study (see Supporting Information). The components with lower BE of Ni  $2p_{3/2}$  (854.2–854.6 eV) origin from the octahedral  $Ni^{2+}$  species found in  $NiCo_2O_4$  and  $Ni(OH)_2$ . In contrast, NiO has much lower BE ~853.7 eV and cannot be considered here. The higher BE species (856.0–856.5 eV) are related to the surface  $Ni^{3+}$  oxyhydroxides [21, 56, 57]. The latter species are dominating in Ni  $2p$  spectra having more than two times larger area than  $Ni^{2+}$  components. It is worth mentioning that metallic component has not been found in our zeolites.

The Co  $2p$  XPS spectra obtained for microporous and mesoporous  $Ni_3Co_{20}$ Beta zeolites are presented in Fig. 3. The main parameters of the fitted components are presented in Table 1. The Co  $2p$  core level spectra are characterized by two doublet components (Co  $2p_{3/2}$  and  $2p_{1/2}$ ) and respective shake-up satellites. The main structures come from the charge-transfer (CT) states  $2p^53d^8L^{-1}$  (L—ligand), whereas

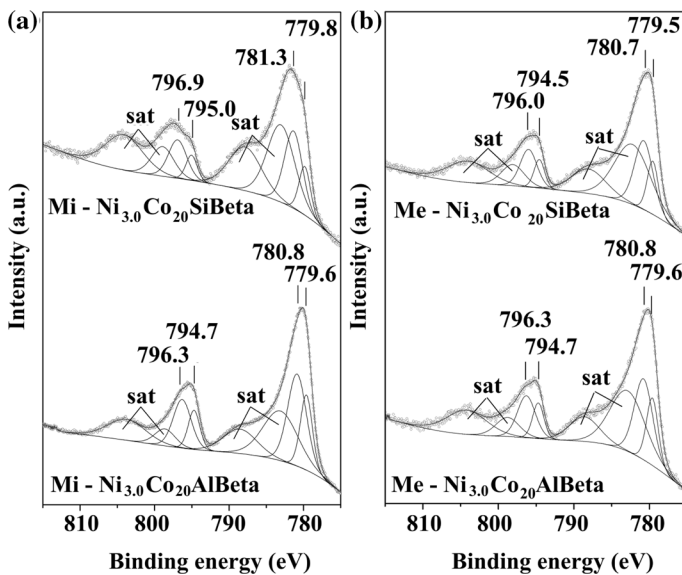


Fig. 3 The Co  $2p$  XPS spectra recorded for Mi– $Ni_{3.0}Co_{20}$ Beta (a) and Me– $Ni_{3.0}Co_{20}$ Beta (b) samples

**Table 1** The BE values (eV) and relative areas of components (%) of Co  $2p_{3/2}$  core excitations obtained for  $\text{Ni}_3\text{Co}_{20}\text{BEA}$  samples. The spin-orbit splitting  $\Delta_{\text{SO}}$  (eV) of each doublet is also listed

Sample	A	B	$\Delta_{\text{SO}}$	Satellites
Mi- $\text{Ni}_3\text{Co}_{20}\text{AlBEA}$	779.6 (34.4)	780.8 (65.6)	15.1 15.5	783.1 788.5
Mi- $\text{Ni}_3\text{Co}_{20}\text{SiBEA}$	779.8 (28.6)	781.3 (71.4)	15.2 15.6	783.0 787.8
Me- $\text{Ni}_3\text{Co}_{20}\text{AlBEA}$	779.6 (34.6)	780.8 (65.4)	15.1 15.5	782.9 788.6
Me- $\text{Ni}_3\text{Co}_{20}\text{SiBEA}$	779.5 (32.0)	780.7 (68.0)	15.0 15.3	782.2 788.0

the satellites reflect non-CT  $2p^53d^7$  states. Latter ones overlap the main lines, which complicates the analysis of spectra shapes, but still they provide some additional arguments useful in characterization of the cobalt chemical environment. It is worth noting that binding energy values of the Co  $2p$  peaks are not always sufficient in identifying the chemical environment of cobalt, since relatively small shifts are reported to. In such case, the distance between two peaks in the doublet (spin-orbit splitting  $\Delta_{\text{SO}}$ ) and the satellite structure are also very informative.

At first glance, the spectra obtained for micro- and mesoporous zeolites are quite similar (Fig. 3), consisting of two Co  $2p_{3/2}$  components at c.a. 779.6 eV and c.a. 780.8 eV binding energies. Their relative intensity ratio does not depend on the development of specific surface area and is close to 1:2, respectively (Table 1). The occurrence of strong satellite lines as well as their BE positions is characteristic of Co(II) in the high-spin state [58, 59]. This finding is also supported by the Co  $2p$  spin-orbit splittings  $\Delta_{\text{SO}}$  of 15.0–15.6 eV belonging to the range characteristic for Co(II). The minor component with BE c.a. 779.6 eV can be identified as coming from Co(II) species in octahedral surroundings. The well-known cobalt oxides in bulk-like form are reported with only slightly larger values: 780.0–780.9 eV for CoO, 779.4–780.1 eV for  $\text{Co}_3\text{O}_4$  and 780.0–780.3 eV for Co(OH)O [56, 60, 61]. Thus, we associate low-BE component with the extra-framework oxides in the form of large clusters or oligonuclear complexes. The dominant component with Co  $2p_{3/2}$  binding energy c.a. 780.8 eV can be identified as coming from tetrahedral Co(II) species embedded into the zeolite matrix [62]. Some more detailed analysis proved that the shape of Mi- $\text{Ni}_3\text{Co}_{20}\text{SiBEA}$  spectrum differs from the others. It is especially well visible in the shape of Co  $2p_{1/2}$  line (Fig. 3). In this case, one can find a BE shift of both Co  $2p$  components to slightly larger values. These can be related to the degree of cations dispersion as well as to the nature of their interactions with the zeolite matrix in which they are embedded. The higher BE for Co(II) might also reflect the occurrence of highly isolated species in this case.

The atomic ratios of cobalt and nickel with respect to silicon for all samples have also been determined and listed in Supporting Information. Data was calculated from the integral intensities of Co  $2p$ , Ni  $2p$  and Si  $2p$  lines with consideration for atomic sensitivity factors. One can find out that Co/Si and Ni/Si ratios for Mi- $\text{Ni}_3\text{Co}_{20}\text{AlBEA}$  sample are roughly two times higher comparing to other samples; nevertheless nominal amounts of metals were initially at the same level.

### The reducibility of Me-Ni<sub>3.0</sub>Co<sub>20</sub>Beta and Mi-Ni<sub>3.0</sub>Co<sub>20</sub>Beta catalysts

Figure 4 shows TPR—H<sub>2</sub> profiles for all samples, where peaks with maximum in the temperature range of 288–390 °C can be seen. Similarly, to Co<sub>x</sub>Beta systems, in the case of bimetallic systems, a multi-stage reduction process is visible [63, 64]. The first peak with a maximum at 288–334 °C may be related to the reduction of the Co<sub>3</sub>O<sub>4</sub> phase and/or NiO localized in the extra-framework positions to CoO and Ni<sup>0</sup>, respectively. In addition, peaks with a maximum temperature range of 336–383 °C are found and it could be assigned to the reduction of CoO to Co<sup>0</sup>. In case of Me-Ni<sub>3.0</sub>Co<sub>20</sub>SiBeta, Mi-Ni<sub>3.0</sub>Co<sub>20</sub>AlBeta, Me-co-Ni<sub>3.0</sub>Co<sub>20</sub>AlBeta and Mi-co-Ni<sub>3.0</sub>Co<sub>20</sub>SiBeta samples, the third reduction peak is observed with the maximum at the temperature of 358–388 °C. Its presence is associated with the reduction of CoO and/or Ni complexes in octahedral coordination [65–68]. Moreover, only for dealuminated samples one can find a high-temperature peak (>730 °C). Its appearance can be attributed to the reduction of hardly reducible cobalt aluminates and/or silicates and/or pseudotetrahedral Co(II) species placed in the zeolite framework [41, 65, 69].

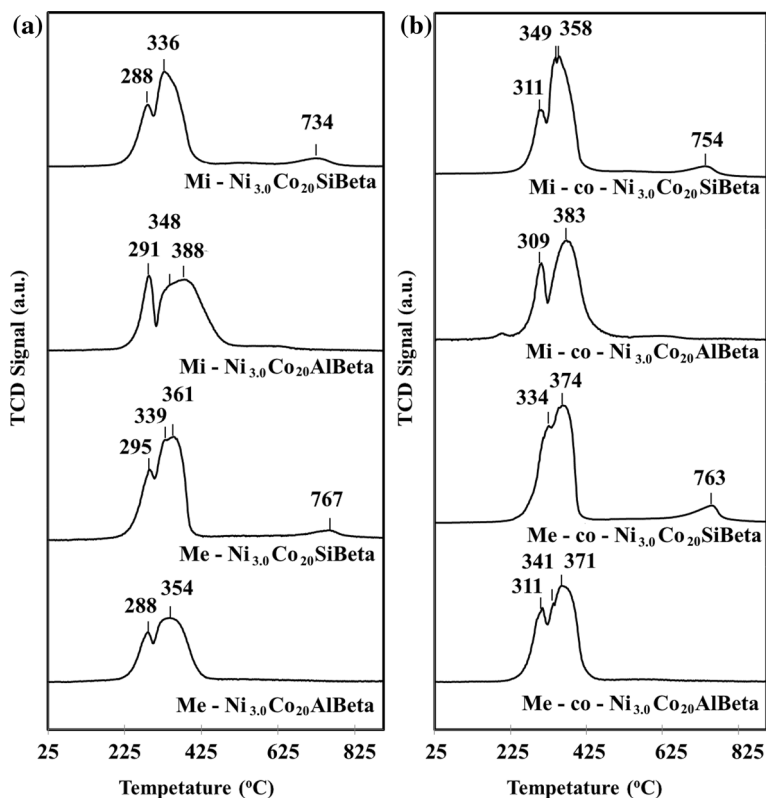


Fig. 4 TPR profiles for Me-Ni<sub>3.0</sub>Co<sub>20</sub>Beta (a) and Mi-Ni<sub>3.0</sub>Co<sub>20</sub>Beta (b) catalysts prepared by sequential impregnation and co-impregnation

The small amount of nickel addition to the cobalt-modified Beta zeolites leads to decrease in the reduction temperature of extra-framework cobalt oxides (reduction temperature is 50 °C lower than in the case of monometallic catalysts) [63, 64]. A similar effect of nickel on reducibility was observed by Rytter et al. [70] for Co/Al<sub>2</sub>O<sub>3</sub> with small addition of nickel catalysts. The authors concluded that the decrease in reduction temperature may be related to the spillover effect or to the formation of a solid solution between the different phases of the cobalt and nickel oxides and support.

### Morphology of bimetallic Me-Ni<sub>3,0</sub>Co<sub>20</sub>Beta and Mi-Ni<sub>3,0</sub>Co<sub>20</sub>Beta catalysts determined by TEM-EDS

TEM characterizations of the four catalysts via TEM images (Fig. 5) pointed out morphological differences characteristic for the two types of supports. The mesoporous samples (Red-Me-co-Ni<sub>3,0</sub>Co<sub>20</sub>SiBEA and Red-Me-co-Ni<sub>3,0</sub>Co<sub>20</sub>AIBEA) include heterogeneous grains in size ranging from 200 nm to more than 1 μm. However, they all have a similar morphology, substantially cubic with a large porosity at the center of each grain. The microporous samples have a less regular morphology comprising grains of various sizes ranging from 50 to 200 nm. All supports are decorated by 10–150 nm nanoparticles, but their dispersion is much better for the mesoporous supports. On the other hand, some agglomerates of nanoparticles as large as 300 nm are well seen for the microporous supports.

The EDX analyzes performed on all samples indicate the presence of Ni and Co elements within the zeolite support. In order to quantify the chemical composition of the nanoparticles for this study, we proceeded to subtract this contribution in the calculations by taking as reference the silicon peak. Thus, for the mesoporous support, the Co/Si ratio is on average twice as high as that for the microporous support (4% against 2%).

The EDX study of mesoporous samples, Red-Me-co-Ni<sub>3,0</sub>Co<sub>20</sub>SiBEA and Red-Me-co-Ni<sub>3,0</sub>Co<sub>20</sub>AIBEA reveals the presence of two groups of particles (Fig. 6). The first group is composed of the particles of large sizes (20–170 nm), which are

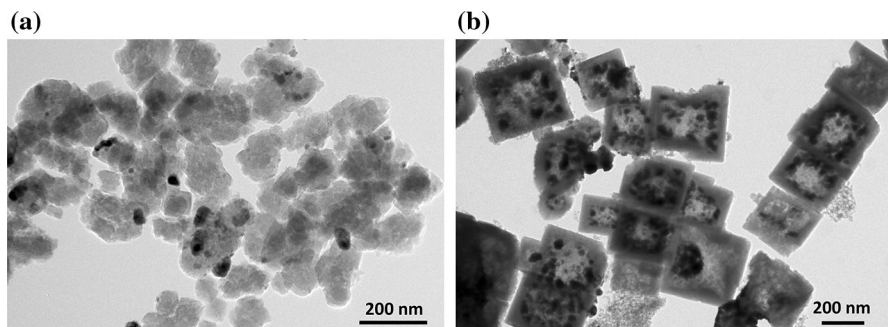


**Fig. 5** TEM micrographs of the Red-Mi-co-Ni<sub>3,0</sub>Co<sub>20</sub>SiBEA (a) and Red-Me-co-Ni<sub>3,0</sub>Co<sub>20</sub>SiBEA (b) catalysts with microporous and mesoporous structure

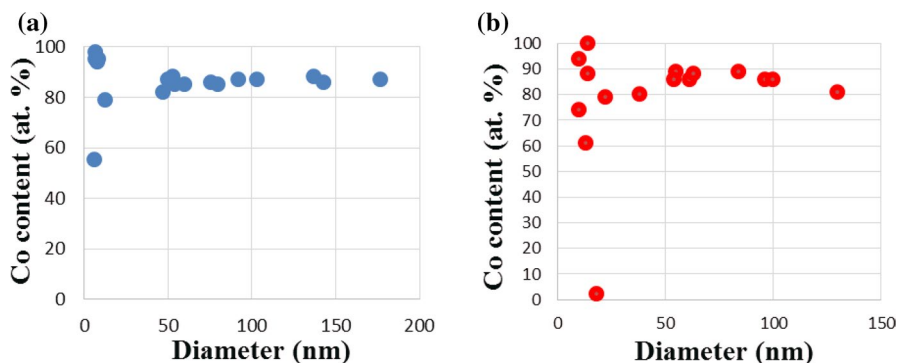


**Fig. 6** Co content (at.%) versus nanoparticles diameter (nm) in the case of the mesoporous Red-Me-co-Ni<sub>3.0</sub>Co<sub>20</sub>SiBEA (a) and Red-Me-co-Ni<sub>3.0</sub>Co<sub>20</sub>AlBEA (b) samples

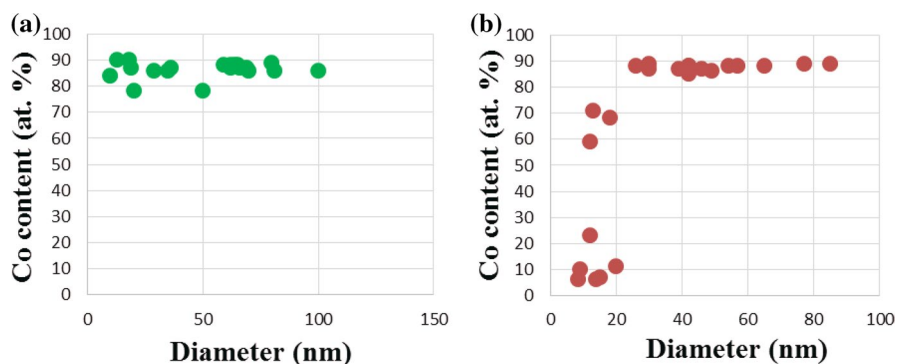


**Fig. 7** Co content (at.%) versus nanoparticles diameter (nm) in the case of the microporous Red-Mi-co-Ni<sub>3.0</sub>Co<sub>20</sub>SiBEA (a) Red-Mi-co-Ni<sub>3.0</sub>Co<sub>20</sub>AlBEA (b) samples

homogeneous in chemical composition with an average of the Co content around 85 at. % inside nanoparticles on both supports. The second group are small particles (<20 nm) whose compositions vary while remaining mainly enriched in Co element.

For microporous Red-Mi-co-Ni<sub>3.0</sub>Co<sub>20</sub>SiBEA and Red-Mi-co-Ni<sub>3.0</sub>Co<sub>20</sub>AlBEA catalysts, the materials have very distinct behavior. In the case of microporous Red-Mi-co-Ni<sub>3.0</sub>Co<sub>20</sub>SiBEA (Fig. 7a), the chemical composition remains homogeneous with a Co content around 88 at. % on all particles measured regardless of their size (10–100 nm). However, for the microporous sample Red-Mi-co-Ni<sub>3.0</sub>Co<sub>20</sub>AlBEA (Fig. 7b), two groups of nanoparticles are again distinguished. The first one consists of large particles (20–100 nm) which are homogeneous in chemical composition with an average Co content around 88 at. % for both supports. The second group are small particles (<20 nm) whose compositions vary with an obvious enrichment in Ni as the size of the studied particles decreases, being able even to reach 95 at. % in Ni content.

### The acidic properties of bimetallic Me–Ni<sub>3.0</sub>Co<sub>20</sub>Beta and Mi–Ni<sub>3.0</sub>Co<sub>20</sub>Beta catalysts determined using TPD–NH<sub>3</sub> method

TPD–NH<sub>3</sub> profiles of nickel–cobalt samples are shown in Fig. 8. For all systems one can distinguish two peaks with maxima in the temperature ranges of 194–232 °C corresponding to weak acid centers, and 405–490 °C corresponding to strong acid centers [65, 71]. Removal of strong acid sites during the dealumination process shifts the low- and high-temperature peaks towards lower temperatures [21, 63, 64]. In addition, the removal of aluminum from the support structure leads to the decreasing of intensity of the low-temperature peak, which is clearly visible in the Ni<sub>3.0</sub>Co<sub>20</sub>SiBeta samples and co-Ni<sub>3.0</sub>Co<sub>20</sub>SiBeta. Introduction of 3 wt% of Ni into the Mi–Co<sub>20</sub>Beta system leads to a shift of the low-temperature peak towards higher temperatures which is most likely related to the formation of new Lewis acid centers [65]. In the case of Me–Ni<sub>3.0</sub>Co<sub>20</sub>Beta and Me-co-Ni<sub>3.0</sub>Co<sub>20</sub>Beta samples, an opposite behavior is observed.

TPD–NH<sub>3</sub> profiles of reduced bimetallic systems are shown in Fig. 9. There are three peaks in the temperature ranges 176–226 °C, 362–379 °C and 418–555 °C for SiBeta support, which can be attributed to weak, medium and strong acid centers, respectively. It can also be seen that the reduction of the co-Ni<sub>3.0</sub>Co<sub>20</sub>Beta and Ni<sub>3.0</sub>Co<sub>20</sub>Beta systems resulted in increasing of intensity of the high-temperature

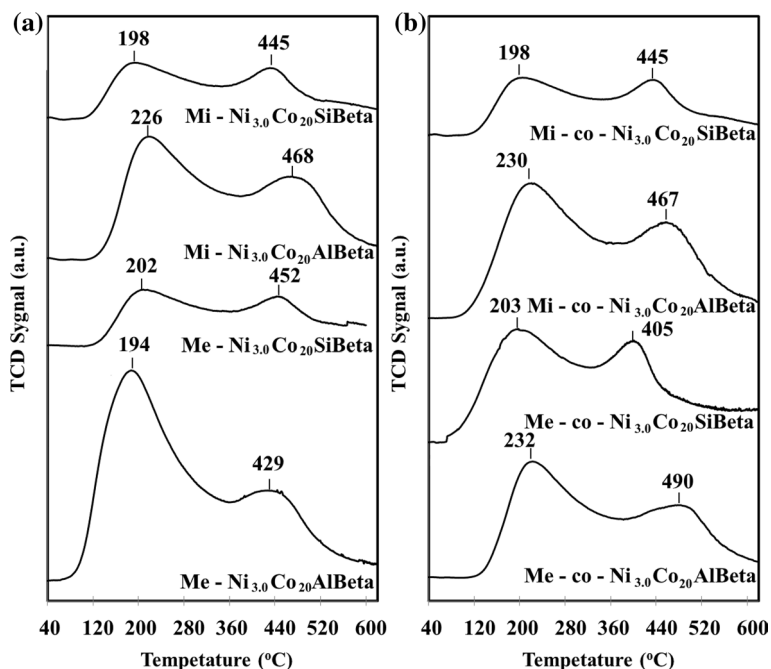


**Fig. 8** TPD profiles for Me–Ni<sub>3.0</sub>Co<sub>20</sub>Beta and Mi–Ni<sub>3.0</sub>Co<sub>20</sub>Beta catalysts prepared by sequential impregnation (a) and co-impregnation (b) after calcination

peak, independently of porosity of supports. The same phenomenon was observed by Stanton et al. [72] who related it to the formation of metallic acid sites.

Table 2 presents the quantitative results of temperature-programmed ammonia desorption. It can be seen that the samples obtained with the two-step post-synthesis method have much smaller number of acid centers than the corresponding samples obtained as a result of wet impregnation. This phenomenon is related to the removal of aluminum atoms from the zeolite structure during the dealumination process. Comparison of the TPD-NH<sub>3</sub> results of Co<sub>3</sub>Beta [63, 64] with bimetallic systems shows that adding nickel to monometallic samples changes their acidity [63, 64]. In the case of Mi-Ni<sub>3.0</sub>Co<sub>20</sub>AlBeta, Me-Ni<sub>3.0</sub>Co<sub>20</sub>AlBeta, Mi-co-Ni<sub>3.0</sub>Co<sub>20</sub>AlBeta and Me-co-Ni<sub>3.0</sub>Co<sub>20</sub>AlBeta, the introduction of nickel increased the amount of adsorbed ammonia indicates the formation of additional adsorption centers.

The reduction of bimetallic systems led to an increase in their acidity, suggesting the formation of new Lewis and/or Brønsted acid centers. However, in the case of Me-Ni<sub>3.0</sub>Co<sub>20</sub>AlBeta, a decrease in the amount of adsorbed ammonia is visible, indicating a reduction in the number of Lewis Co(II) acid centers and the formation of Co nanoparticles.

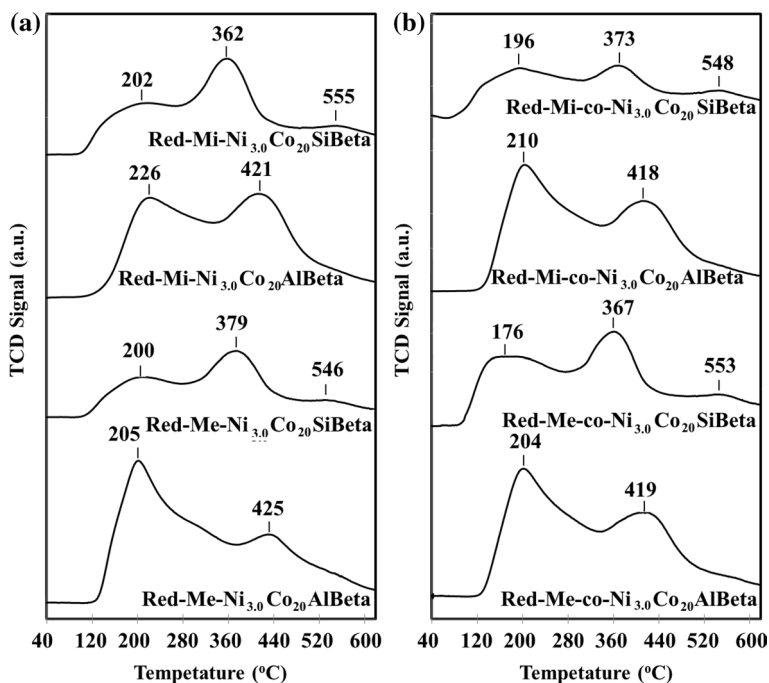


**Fig. 9** TPD profiles for Me-Ni<sub>3.0</sub>Co<sub>20</sub>Beta and Mi-Ni<sub>3.0</sub>Co<sub>20</sub>Beta catalysts prepared by sequential impregnation (a) and co-impregnation (b) after reduction

**Table 2** The amount of adsorbed ammonia calculated based on TPD data

Sample	After the calcination	After the reduction
	Total amount of NH <sub>3</sub> (μmol g <sup>-1</sup> )	Total amount of NH <sub>3</sub> (μmol g <sup>-1</sup> )
Mi-Ni <sub>3,0</sub> Co <sub>20</sub> AlBeta	1455	1817
Mi-co-Ni <sub>3,0</sub> Co <sub>20</sub> AlBeta	1664	1855
Mi-Ni <sub>3,0</sub> Co <sub>20</sub> SiBeta	734	1126
Mi-co-Ni <sub>3,0</sub> Co <sub>20</sub> SiBeta	750	893
Me-Ni <sub>3,0</sub> Co <sub>20</sub> AlBeta	2057	1894
Me-co-Ni <sub>3,0</sub> Co <sub>20</sub> AlBeta	1257	1841
Me-Ni <sub>3,0</sub> Co <sub>20</sub> SiBeta	522	928
Me-co-Ni <sub>3,0</sub> Co <sub>20</sub> SiBeta	1069	1453

### Catalytic activity of bimetallic Me-NiCoBeta and Mi-NiCoBeta catalysts in Fischer-Tropsch synthesis

The conversion of CO and selectivity towards methane, carbon dioxide and liquid products in the presence of the mesoporous and microporous Red-Ni<sub>3,0</sub>Co<sub>20</sub>Beta and Red-co-Ni<sub>3,0</sub>Co<sub>20</sub>Beta catalysts are shown in Figs. 10 and 11.

For Red-Mi-Ni<sub>3,0</sub>Co<sub>20</sub>SiBeta and Red-Me-Ni<sub>3,0</sub>Co<sub>20</sub>SiBeta catalysts, prepared by sequential impregnation the selectivity towards liquid products is high (67.6–68.9%), but with significantly lower CO conversion (80.4–81.0%) than for monometallic cobalt zeolite catalysts [63, 64] and bimetallic nickel-cobalt zeolite catalysts with lower amount of cobalt (Ni<sub>3,0</sub>Co<sub>10</sub>Beta) which activity was described in our earlier work [21]. In the case of samples obtained by co-impregnation, the most active catalysts are Red-Mi-co-Ni<sub>3,0</sub>Co<sub>20</sub>SiBeta and Red-Me-co-Ni<sub>3,0</sub>Co<sub>20</sub>SiBeta. They show very high CO conversion and selectivity to liquid products of 75.1–99.9%. Both Red-Mi-co-Ni<sub>3,0</sub>Co<sub>20</sub>AlBeta and Red-Me-co-Ni<sub>3,0</sub>Co<sub>20</sub>AlBeta show lower CO conversion (18.5–26.7%), but a comparable selectivity to liquid hydrocarbons (73.8–82.8%). This phenomenon was also observed for co-Ni<sub>3,0</sub>Co<sub>10</sub>Beta samples described in our first paper related to bimetallic Beta zeolite catalysts for FTS [21]

It is worth mentioning that all bimetallic samples, except for Red-Me-Ni<sub>3,0</sub>Co<sub>20</sub>SiBeta and Mi-co-Ni<sub>3,0</sub>Co<sub>20</sub>AlBeta, show higher CO conversion than Red-Co<sub>x</sub>Beta monometallic catalysts [63, 64]. Similar observation was noticed by Wang et al. [73] for Co/HZSM-5 catalysts promoted with Ni and Ru. The authors linked this phenomenon with the increase in the degree of CO hydrogenation, which is a consequence of the creation of more available Co<sup>0</sup> active sites. Moreover, after 24 h of reaction in the presence of Red-co-Ni<sub>3,0</sub>Co<sub>20</sub>SiBeta and Red-Mi-co-Ni<sub>3,0</sub>Co<sub>20</sub>AlBeta the formation of carbon dioxide (IV) is not observed.

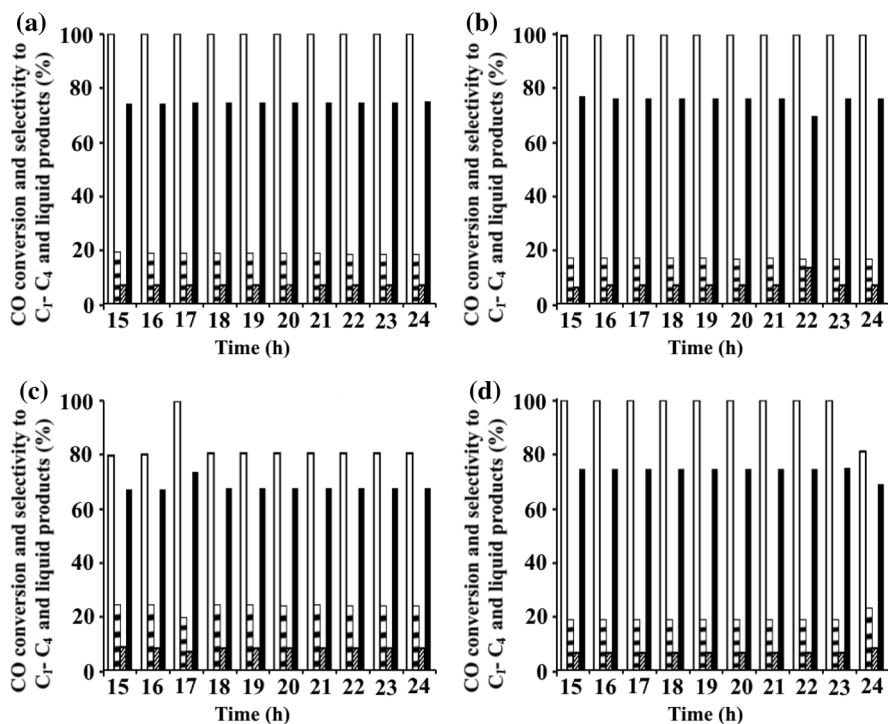


**Fig. 10** Conversion of CO (□) and selectivity to C<sub>1</sub>-C<sub>4</sub> (■), CO<sub>2</sub> (▨) and liquid products (■) after Fischer-Tropsch synthesis ( $T=260\text{ }^{\circ}\text{C}$ ,  $p=30\text{ atm}$ ,  $t=24\text{ h}$ ) over **a** Red-Mi-Ni<sub>3.0</sub>Co<sub>20</sub>AlBeta, **b** Red-Me-Ni<sub>3.0</sub>Co<sub>20</sub>AlBeta, **c** Red-Mi-Ni<sub>3.0</sub>Co<sub>20</sub>SiBeta, **d** Red-Me-Ni<sub>3.0</sub>Co<sub>20</sub>SiBeta (prepared by sequential impregnation)

In the case of the remaining catalysts, the selectivity to carbon dioxide is about 8.2–6.5%. The addition of nickel causes the decrease in selectivity towards liquid products, at the same time leads to an increase in the selectivity towards methane. This may be related to the good ability of this metal to break C–C bonds [73]. The same tendency was observed by Shimura et al. [74] on Ni/Co/HZSM-5 catalysts.

The catalytic activity of all Ni<sub>3.0</sub>Co<sub>20</sub>Beta and co-Ni<sub>3.0</sub>Co<sub>20</sub>Beta catalysts remained stable and on the same level as the bimetallic Beta zeolite catalysts with lower Co content studied in our previous work [21]. According to Ritter et al. [70], the high stability of nickel–cobalt systems may be due to the spillover effect which reduces active phase re-oxidation, sintering and carbon formation on the catalyst surface. In addition, the authors also pointed out that the presence of Ni on the surface of the cobalt system may hinder the formation of graphite carbon which also delays catalyst deactivation.

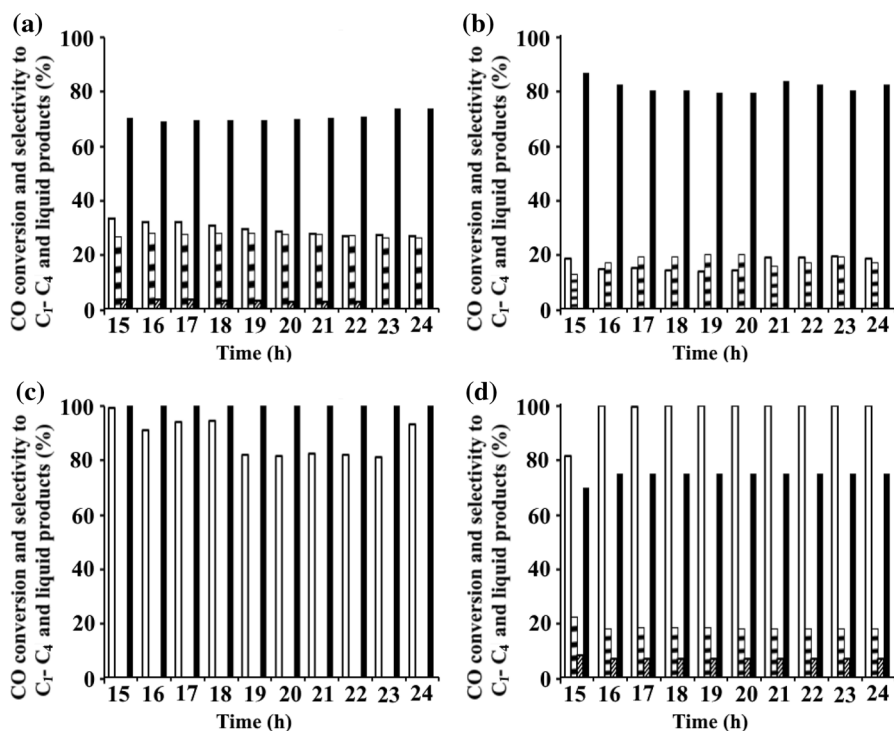


**Fig. 11** Conversion of CO (□) and selectivity to C<sub>1</sub>-C<sub>4</sub> (■), CO<sub>2</sub> (▨) and liquid products (■) after Fischer-Tropsch synthesis ( $T=260$  °C,  $p=30$  atm,  $t=24$  h) over **a** Red-Mi-co-Ni<sub>3.0</sub>Co<sub>20</sub>AlBeta, **b** Red-Me-co-Ni<sub>3.0</sub>Co<sub>20</sub>AlBeta, **c** Red-Mi-co-Ni<sub>3.0</sub>Co<sub>20</sub>SiBeta, **d** Red-Me-co-Ni<sub>3.0</sub>Co<sub>20</sub>SiBeta (prepared by co-impregnation)

## Conclusion

For Red-Mi-Ni<sub>3.0</sub>Co<sub>20</sub>SiBeta and Re-Me-Ni<sub>3.0</sub>Co<sub>20</sub>SiBeta samples obtained during sequential impregnation, the increase in selectivity towards liquid products was noted but also significantly decrease in CO conversion in contrary to samples prepared by co-impregnation for which the high selectivity and CO conversion was found.

It is also worth mentioned that dealumination process, the same as for monometallic CoBeta catalysts and bimetallic Ni<sub>3.0</sub>Co<sub>10</sub>Beta catalysts, improves their activity in FTS. It may be related to decreasing the acidity, stronger interactions of Co species with structure of Beta zeolites and formation of new acidic and active sites.

The presented studies showed that the use of a two-step post-synthesis method and the promotion of cobalt systems with nickel allow to obtain active, selective, and stable zeolite catalysts for Fischer-Tropsch synthesis. These promising results encourage to continue this study, and to undertake further attempts to improve the catalytic properties of the described zeolite materials in the Fischer-Tropsch process.

## Memory with Prof. Michel Che

With the present contribution we would like to pay a tribute to Prof. Michel Che and our long-lasting friendship and collaboration with more than 45 publication by adding yet another chapter on nickel-cobalt zeolite catalysts applied for the Fischer-Tropsch synthesis. The challenge was to prepare cobalt systems promoted with nickel allow to obtain active, selective, and stable catalysts for Fischer—Tropsch synthesis.



Photo: Professor Michel Che with Profs Helmut Knözinger, Konstantin Hadjiivanov and Stanislaw Dzwigaj (from left to right) during 23rd Annual Conference of Academia Europaea organized on September 22nd 2011 in UNESCO Headquarters, Paris.

## References

1. K.K. Ramasamy, M. Gray, H. Job, Y. Wang, *Chem. Eng. Sci.* **135**, 266 (2015)
2. J.-I. Yang, C.H. Ko, *Res. Chem. Intermed.* **45**, 4417 (2019)
3. V.Z. Mordkovich, V.S. Ermolaev, E.B. Mitberg, L.V. Sineva, I.G. Solomonik, I.S. Ermolaev, E.Y. Asalieva, *Res. Chem. Intermed.* **41**, 9539 (2015)
4. Y. Traa, *Chem. Comm.* **46**, 2175 (2010)
5. M.E. Dry, *Appl. Catal. A* **276**, 1 (2004)
6. A.A. Mirzaei, M.K. Rouhoullah, H. Atashi, M. Arsalanfar, S. Shahriari, *J. Indus. Eng. Chem.* **18**, 1242 (2012)
7. M. Ding, Y. Yang, J. Xu, Z. Tao, H. Wang, H. Wang, H. Xiang, Y. Li, *Appl. Catal. A* **345**, 176 (2008)
8. G.P.V. Laan, A.A.C.M. Beenackers, *Catal. Rev. Sci. Eng.* **41**, 255 (1999)
9. F.G. Botes, B.B. Breman, *Indus. Eng. Chem. Res.* **45**, 7415 (2006)
10. M.E. Dry, *Catal. Today* **71**, 227 (2002)
11. M. Sarkari, F. Fazlollahi, H. Atashi, A.A. Mirzaei, V. Hosseinpour, *Fuel Proc. Tech.* **97**, 130 (2012)
12. T. Li et al., *Fuel Proc. Tech.* **118**, 117 (2014)

13. L. Spadaro, F. Arena, M.L. Granados, M. Ojeda, J.L.G. Fierro, F. Frusteri, *J. Catal.* **234**, 451 (2005)
14. T.M. Katsuya Shimura, T. Hanaoka, S. Hirata, *J. Mol. Catal. A* **407**, 15 (2015)
15. A.A.M.P. Nikparsaa, H. Atashib, *J. Fuel Chem. Tech.* **42**, 710 (2014)
16. S. Iqbal, T.E. Davies, D.J. Morgan, K. Karim, J.S. Hayward, J.K. Bartley, S.H. Taylor, G.J. Hutchings, *Catal. Today* **275**, 35 (2016)
17. V.R. Calderone, N.R. Shiju, D.C. Ferré, G. Rothenberg, *Green Chem.* **13**, 1950 (2011)
18. P. van Helden, F. Prinsloo, J.-A. van den Berg, B. Xaba, W. Erasmus, M. Claeys, J. van de Loosdrecht, *Catal. Today* **342**, 88 (2019)
19. H. Yu, A. Zhao, H. Zhang, W. Ying, D. Fang, *Ener. Sour. A Recov. Utiliz. Environ. Eff.* **37**, 47 (2015)
20. N.Y. Kim, J.-S. Jung, J.S. Lee, E.H. Yang, G.H. Hong, S.S. Lim, Y.S. Noh, J.L. Hodala, K.Y. Lee, D.J. Moon, *Res. Chem. Intermed.* **42**, 319 (2016)
21. R. Sadek, K.A. Chalupka, P. Mierczynski, W. Maniukiewicz, J. Rynkowski, J. Gurgul, M. Lasoń-Rydel, S. Dzwigaj, *Catalysts* **10**, 112 (2020)
22. S. Dzwigaj, M.J. Peltre, P. Massiani, A. Davidson, M. Che, T. Sen, S. Sivasanker, *Chem. Commun.* **87** (1998)
23. S. Dzwigaj, P. Massiani, A. Davidson, M. Che, *J. Mol. Catal.* **155**, 169 (2000)
24. R. Hajjar, Y. Millot, P.P. Man, M. Che, S. Dzwigaj, *J. Phys. Chem. C* **112**, 20167 (2008)
25. S. Dzwigaj, M. Matsuoka, M. Anpo, M. Che, *Res. Chem. Intermed.* **29**, 665 (2003)
26. M. Anpo, S. Dzwigaj, M. Che, *Adv. Catal.* **52**, 1 (2009)
27. S. Dzwigaj, M. Matsuoka, R. Franck, M. Anpo, M. Che, *J. Phys. Chem. B* **102**, 6309 (1998)
28. S. Dzwigaj, M. Matsuoka, M. Anpo, M. Che, *J. Phys. Chem. B* **104**, 6012 (2000)
29. S. Dzwigaj, M. Che, *J. Phys. Chem. B* **110**, 12490 (2006)
30. J. Janas, T. Machej, J. Gurgul, R.P. Socha, M. Che, S. Dzwigaj, *Appl. Catal. B* **75**, 239 (2007)
31. S. Dzwigaj, J. Janas, T. Machej, M. Che, *Catal. Today* **119**, 133 (2007)
32. J. Janas, J. Gurgul, R.P. Socha, T. Shishido, M. Che, S. Dzwigaj, *Appl. Catal. B* **91**, 113 (2009)
33. S. Dzwigaj, J. Janas, J. Gurgul, R.P. Socha, T. Shishido, M. Che, *Appl. Catal. B* **85**, 131 (2009)
34. J. Janas, J. Gurgul, R.P. Socha, J. Kowalska, K. Nowinska, T. Shishido, M. Che, S. Dzwigaj, *J. Phys. Chem. C* **113**, 13273 (2009)
35. J.P. Nogier, Y. Millot, P.P. Man, T. Shishido, M. Che, S. Dzwigaj, *J. Phys. Chem.* **113**, 4885 (2009)
36. S. Dzwigaj, M. Che, *Catal. Today* **169**, 232 (2011)
37. R. Baran, T. Onfroy, S. Casale, S. Dzwigaj, *J. Phys. Chem. C* **118**, 20445 (2014)
38. R. Baran, J.-M. Krafft, T. Onfroy, T. Grzybek, S. Dzwigaj, *Micropor. Mesopor. Mater.* **225**, 515 (2016)
39. F. Fazlollahi, M. Sarkari, A. Zare, A.A. Mirzaei, H. Atashi, *J. Ind. Eng. Chem.* **18**, 1223 (2012)
40. B. Erdogan, H. Arbag, N. Yasyerli, *Int. J. Hydrogen Energy* **43**, 1396 (2018)
41. A. Mosayebi, R. Abedini, *Int. J. Hydrogen Energy* **42**, 27013 (2017)
42. A. Rodriguez-Gomez, A. Caballero, *Mol. Catal.* **449**, 122 (2018)
43. H. Arbag, S. Yasyerli, N. Yasyerli, G. Dogu, T. Dogu, *Appl. Catal. B* **198**, 254 (2016)
44. P. Boroń, L. Chmielarz, J. Gurgul, K. Łątka, T. Shishido, J.-M. Krafft, S. Dzwigaj, *Appl. Catal. B* **138–139**, 434 (2013)
45. P. Boroń, L. Chmielarz, J. Gurgul, K. Łątka, B. Gil, J.-M. Krafft, S. Dzwigaj, *Catal. Today* **235**, 210 (2014)
46. I. Kocemba, J. Rynkowski, J. Gurgul, R.P. Socha, K. Łątka, J.-M. Krafft, S. Dzwigaj, *Appl. Catal. A* **519**, 16 (2016)
47. M.S. Kumar, M. Schwidder, W. Grünert, U. Bentrup, A. Brückner, *J. Catal.* **239**, 173 (2006)
48. K. Arishtirova, P. Kovacheva, A. Predoeva, *Appl. Catal. A* **243**, 191 (2003)
49. P. Kovacheva, K. Arishtirova, A. Predoeva, *React. Kin. Catal. Lett.* **79**, 149 (2003)
50. L.P. Oleksenko, *Theoret. Exper. Chem.* **40**, 331 (2004)
51. W. Grünert, R. Schlögl, *Mol. Sieves* **4**, 467 (2004)
52. NIST X-ray Photoelectron Spectroscopy Database.
53. J. Janas, J. Gurgul, R.P. Socha, S. Dzwigaj, *Appl. Catal. B* **91**, 217 (2009)
54. J. Gurgul, K. Łątka, I. Hnat, J. Rynkowski, S. Dzwigaj, *Micropor. Mesopor. Mater.* **168**, 1 (2013)
55. P. Boroń, L. Chmielarz, J. Gurgul, K. Łątka, B. Gil, B. Marszałek, S. Dzwigaj, *Micropor. Mesopor. Mater.* **203**, 73 (2015)
56. J.-G. Kim, D.L. Pugmire, D. Battaglia, M.A. Langell, *Appl. Sur. Sci.* **165**, 70 (2000)
57. J.L. Rodríguez, M.A. Valenzuela, T. Poznyak, L. Lartundo, I. Chairez, J. Hazard, *Mater.* **262**, 472 (2013)
58. R.J.O. Mossaneck, I. Preda, M. Abbate, J. Rubio-Zuazo, G.R. Castro, A. Vollmer, A. Gutierrez, L. Soriano, *Chem. Phys. Lett.* **501**, 437 (2011)
59. A. P. Grosvenor, M. C. Biesinger, R. St. C. Smart, N. S. McIntyre, *Surf. Sci.* **600**, 1771 (2006)
60. B. P. Payne, X-ray Photoelectron Spectroscopy Studies on the Oxidation Processes of Nickel, Chromium and their Alloys. Electronic Thesis and Dissertation Repository. 201 (2011)

61. D. Briggs, V.A. Gibson, *Chem. Phys. Lett.* **25C**, 493 (1974)
62. Y. Okamoto, H. Nakano, T. Imanaka, *Bull. Chem. Soc. Jpn.* **48**, 2163 (1975)
63. R. Sadek, K.A. Chalupka, P. Mierczynski, J. Rynkowski, J. Gurgul, S. Dzwigaj, *Catalysts* **9**, 497 (2019)
64. R. Sadek, K.A. Chalupka, P. Mierczynski, J. Rynkowski, Y. Millot, L. Valentin, S. Casale, S. Dzwigaj, *Catal. Today* **354**, 109 (2020)
65. K.A. Chalupka, S. Casale, E. Zurawicz, J. Rynkowski, S. Dzwigaj, *Micropor. Mesopor. Mat.* **211**, 9 (2015)
66. K.A. Chalupka, W.K. Jozwiak, J. Rynkowski, W. Maniukiewicz, S. Casale, S. Dzwigaj, *Appl. Catal. B* **146**, 227 (2014)
67. T.H. Lim, S.J. Cho, H.S. Yang, M.H. Engelhard, D.H. Kim, *Appl. Catal. A* **505**, 62 (2015)
68. A. Nieto-Márquez, J.C. Lazo, A. Romero, J.L. Valverde, *Chem. Eng. J.* **144**, 518 (2008)
69. C. Ochoa-Hernández, Y. Yang, P. Pizarro, V.A. de la Peña O'Shea, J.M. Coronado, D.P. Serrano, *Catal. Today* **210**, 81 (2013)
70. E. Rytter, T.H. Skagseth, S. Eri, A.O. Sjøstad, *Ing. Eng. Chem. Res.* **49**, 4140 (2010)
71. F. Tian, Y. Wu, Q. Shen, X. Li, Y. Chen, C. Meng, *Micropor. Mesopor. Mater.* **173**, 129 (2013)
72. A.R. Stanton, K. Iisa, M.M. Yung, K.A. Magrini, *J. Anal. Appl. Pyrol.* **135**, 199 (2018)
73. S. Wang, Q. Yin, J. Guo, B. Ru, L. Zhu, *Fuel* **108**, 597 (2013)
74. K. Shimura, T. Miyazawa, T. Hanaoka, S. Hirata, *J. Mol. Catal. A* **407**, 15 (2015)

**Publisher's Note** Springer Nature remains neutral with regard to jurisdictional claims in published maps and institutional affiliations.



K. A. Chalupka



R. Sadek



J. Rynkowski



J. Gurgul



D. Broui



S. Dzwigaj

## Authors and Affiliations

**Karolina A. Chalupka<sup>1</sup> · Renata Sadek<sup>1,2</sup> · Lukasz Szkudlarek<sup>1</sup> ·  
Pawel Mierczynski<sup>1</sup> · Waldemar Maniukiewicz<sup>1</sup> · Jacek Rynkowski<sup>1</sup> ·  
Jacek Gurgul<sup>3</sup> · Sandra Casale<sup>2</sup> · Dalil Brouri<sup>2</sup> · Stanislaw Dzwigaj<sup>2</sup>**

Renata Sadek  
renata.sadek90@gmail.com

Pawel Mierczynski  
pawel.mierczynski@p.lodz.pl

Waldemar Maniukiewicz  
waldemar.maniukiewicz@p.lodz.pl

Jacek Rynkowski  
jacek.rynkowski@p.lodz.pl

Jacek Gurgul  
ncgurgul@cyf-kr.edu.pl

Sandra Casale  
sandra.casale@sorbonne-universite.fr

Dalil Brouri  
dalil.brouri@sorbonne-universite.fr

- <sup>1</sup> Institute of General and Ecological Chemistry, Lodz University of Technology, Zeromskiego 116, 90-924 Lodz, Poland
- <sup>2</sup> Laboratoire de Réactivité de Surface, Sorbonne Université-CNRS, UMR 7197, 4 Place Jussieu, Case 178, 75252 Paris, France
- <sup>3</sup> Jerzy Haber Institute of Catalysis and Surface Chemistry, Polish Academy of Sciences, Niezapominajek 8, 30239 Krakow, Poland